PHYSICAL REVIEW C VOLUME 29, NUMBER 3 MARCH 1984

Angular momentum projection on a mesh of cranked Hartree-Fock wave functions

D. Baye and P.-H. Heenen
Physique Théorique et Mathématique, Université Libre de Bruxelles, B-1050 Bruxelles, Belgium

(Received 28 October 1983)

A method for projecting on angular momentum wave functions discretized on a three-dimensional Cartesian mesh is presented. The method is based on a matrix representation of the rotation operator. It is applied to cranked Hartree-Fock wave functions calculated for ^{24}Mg with a simple interaction. In this case, the accuracy of the projected matrix elements is estimated to be of the order of 0.1%. An extensive comparison of the projected and cranking energies is made. The validity of the cranking method as an approximation to a variation-after-projection calculation seems to be wider than usually expected. The study of the fission barrier of ^{24}Mg for the channel ^{4}He-^{16}O-^{4}He shows that the cranking predictions for these very deformed states are quite reliable.

I. INTRODUCTION

A large number of self-consistent calculations of nuclear properties have been performed in the last few years.[1] They have been mainly devoted to the study of intrinsic nuclear states. It is well known that the Slater determinants determined in this way violate most of the symmetries of the nuclear Hamiltonian.[2] The restoration of rotational invariance requires in principle a variation after projection on angular momentum (VAP) of the trial functions. Calculations of this type have been performed for a few light nuclei.[3,4] The Hartree-Fock (HF) equations are constrained on one or a few collective degrees of freedom (usually the quadrupole moment) and the resulting wave functions are projected on angular momentum. Although the variational space has always been very restricted, the intrinsic state has been found to change as a function of angular momentum along a band.[3,4] Together with the angular-momentum projection, the variation makes the calculation extremely tedious.

The cranking method provides an interesting alternative to a VAP calculation. It can be demonstrated[5] that within a band, the relative energies calculated by the cranking prescription are a good approximation to the VAP energies provided that three conditions are fulfilled: (i) The nucleus is nearly axial. This is equivalent to the requirement that the dispersion in angular momentum in one direction is very small

$$\langle (\Delta\hat{L}_z)^2\rangle \approx 0\ . \qquad (1.1a)$$

(ii) The deformation is strong

$$\langle (\Delta\hat{L}_y)^2\rangle \gg 1\ . \qquad (1.1b)$$

(iii) The trial function $|\Psi\rangle$ has a definite signature

$$e^{i\pi\hat{L}_x}|\Psi\rangle = \pm|\Psi\rangle\ . \qquad (1.1c)$$

The cranked Hartree-Fock Bogoliubov (CHFB) method has been used with considerable success for the description of high spin states in the rare-earth region (see the references in Ref. 6). For these deformed heavy nuclei, the conditions of validity of the cranking approximation are well fulfilled except in the backbending region. Hara *et al.*[6] have recently performed a numerical test of this validity by projecting CHFB wave functions on angular momentum. They have confirmed the general trends of the results of the cranking method, although the moment of inertia of the ground state band is decreased by a factor of 1.3.

The cranking method has also been extensively used to describe light nuclei with Nilsson[7] or Hartree-Fock wave functions.[8,9] In these calculations, a large number of rotational bands are obtained. They correspond to different energy minima as a function of the deformation, some of them being even triaxial. The HF calculation of Refs. 8 and 9 have been performed with a new technique derived from time-dependent Hartree-Fock (TDHF) calculations.[10] The individual wave functions are discretized on a three-dimensional Cartesian mesh and the HF equations are solved on this mesh. This technique enables one to avoid all the difficulties associated with the choice of a basis and with its truncation. In particular, very different configurations of a nucleus can be described on the same mesh, while a unique basis is not adequate for that purpose. The use of a simple Skyrme-type interaction without spin orbit, the Bonche-Koonin-Negele (BKN) + Coulomb interaction,[1] has permitted one to study a very large number of bands leading to different fission modes. Unfortunately, the validity of the cranking approximation is not established and is probably not uniform for all the bands determined for these light nuclei.

In this paper, we develop a new method for the projection of wave functions discretized on a mesh. This method is very general and can be applied to any type of wave function and nuclear interaction (including spin orbit). It is based on the properties of discretized forms of the angular momentum operators on a mesh. In the following, we shall restrict ourselves to Slater determinants having the symmetries imposed in Ref. 8 and to the BKN + Coulomb interaction. The implementation of these symmetries and the use of a simple interaction will enable us to study in detail the effect of projection on cranked ^{24}Mg wave functions.

In Sec. II, we summarize the cranked HF model with emphasis on the symmetries imposed in Ref. 8 on the wave functions of the model. We also show the consequences of these symmetries on the projection method. In Sec. III, we state the method used to rotate wave functions on a mesh and discuss its accuracy through examples. In Sec. IV, the method is applied to ^{24}Mg cranked HF wave functions and discussed. The yrast line and fission barrier are studied. Conclusions are presented in Sec. V.

II. SUMMARY OF THE THEORY

A. The cranked Hartree-Fock model

The cranked Hartree-Fock wave function $|\Psi_\omega\rangle$ is a Slater determinant minimizing the expectation value

$$E_\omega = \langle \Psi_\omega | \hat{H} - \omega \hat{L}_x | \Psi_\omega \rangle \ , \tag{2.1}$$

for a given value of the Lagrange parameter ω. We have introduced in (2.1) the total orbital momentum $\hat{L}_x$ in place of the total angular momentum $\hat{J}_x$ since we shall be dealing with spin-scalar forces.[11] The generalization to the case of $\hat{J}_x$ would be straightforward. Under conditions (1.1), Eq. (2.1) has been shown to provide an approximation of a VAP calculation.[5] The interesting physical quantity is the energy

$$E = \langle \Psi_\omega | \hat{H} | \Psi_\omega \rangle = E_\omega + \omega L_x \ , \tag{2.2}$$

with $L_x = \langle \hat{L}_x \rangle$. Since $\hat{L}_x$ changes sign under time reversal $\hat{T}$, the wave functions obtained from (2.1) are not invariant under $\hat{T}$

$$\hat{T} | \Psi_\omega \rangle = | \Psi_\omega \rangle^* = | \Psi_{-\omega} \rangle \ , \tag{2.3}$$

but the time-reversed wave function leads to the same energies E and E_ω.

Both $\hat{H}$ and $\hat{L}_x$ commute with parity $\hat{P}$ and with reflection $\hat{P}_x$ through the *yz* plane. The cranked wave functions are chosen as in Refs. 8 and 9 to be eigenfunctions of the symmetry operators

$$\hat{P} | \Psi_\omega \rangle = \Pi | \Psi_\omega \rangle \ , \tag{2.4a}$$

$$\hat{P}_x | \Psi_\omega \rangle = \Pi_x | \Psi_\omega \rangle \ , \tag{2.4b}$$

with $|\Pi| = |\Pi_x| = 1$. From (2.4b) follows the well-known property $\langle \hat{L}_y \rangle = \langle \hat{L}_z \rangle = 0$. A further symmetry restriction is conserved in the cranking model[12] and is imposed on the wave functions

$$\hat{T}\hat{P}_z | \Psi_\omega \rangle = | \Psi_\omega \rangle \ . \tag{2.4c}$$

The three symmetry operations applied to the real or imaginary part of $|\Psi_\omega\rangle$ belong to the D_{2h} group.[13] They restrict the variational space. Moreover, the calculations of matrix elements can be performed over one-eighth of the configuration space,[8] which reduces the computation times. The exploitation of the symmetries will also reduce the rotation times and thus the whole projection process (see Sec. III).

In practice, for $4N$ nuclei studied with the BKN force as in Refs. 8 and 9, a spin-isospin degeneracy is imposed. Coulomb terms are treated in the equal-$\frac{1}{2}e$-charge approximation. The spin-isospin degeneracy restricts the values of Π and Π_x to $+1$. Hence, the real and imaginary parts of $|\Psi_\omega\rangle$ transform, respectively, according to the A_g and B_{3g} irreducible representations (IR) of D_{2h} (Ref. 13) and are thus orthogonal. The symmetries (2.4) can also be imposed on the individual wave functions ψ_i. The individual wave functions can be partitioned into four mutually orthogonal blocks according to their symmetries. The real or imaginary part of ψ_i corresponds to one of the eight IR's of D_{2h}. Therefore, matrix elements involving individual wave functions whose real or imaginary parts do not belong to the same block, vanish.

B. Angular-momentum projection

For triaxially deformed wave functions, the general form of the projection operator has to be used in order to restore the angular momentum quantum number L and its projection M. The projection operator selects components with a given angular momentum from the expansion of the cranked HF wave function

$$|\Psi_\omega\rangle = \sum_{\lambda L K} a_{\lambda L K} | \lambda L K \rangle \ . \tag{2.5}$$

The projected wave function is defined by

$$|\Psi_K^{LM}\rangle = \frac{2L+1}{8\pi^2} \int D_{MK}^{L*}(\Omega) \hat{R}(\Omega) | \Psi_\omega \rangle d\Omega \ . \tag{2.6}$$

In (2.6), Ω represents the three Euler angles α, β, and γ; D_{MK}^{L} is a Wigner function; and $\hat{R}(\Omega)$ is the rotation operator

$$\hat{R}(\Omega) = e^{i\alpha\hat{L}_z} e^{i\beta\hat{L}_y} e^{i\gamma\hat{L}_z} \ . \tag{2.7}$$

The insertion of (2.5) in (2.6) provides the expression

$$|\Psi_K^{LM}\rangle = \sum_{\lambda} a_{\lambda L K} | \lambda L M \rangle \ , \tag{2.8}$$

which shows that K is not a good quantum number.

The preceding equations are well known; let us specialize them to an intrinsic state $|\Psi_\omega\rangle$ exhibiting the symmetries (2.4). The relations

$$a_{\lambda L K}^* = (-)^L a_{\lambda L -K} = \Pi_x a_{\lambda L K} \tag{2.9}$$

are readily shown using (2.4b), (2.4c), and (2.5). They prove that the coefficients $a_{\lambda L K}$ are real or imaginary. For $K \neq 0$, the states corresponding to $+K$ and $-K$ are linearly dependent. For $K=0$, the states for which L fulfills $(-)^{L+1} = \Pi_x$ are forbidden. Moreover, (2.4c) and (2.5) show that for $\Pi = +1$ the even-K components belong to the real part of $|\Psi_\omega\rangle$ and the odd-K ones belong to its imaginary part.

Since K is not a good quantum number, the best projected state $|\Psi^{LM}\rangle$ which can be obtained from $|\Psi_\omega\rangle$ is given by

$$|\Psi^{LM}\rangle = \sum_{K \geq 0} g_K | \Psi_K^{LM} \rangle \ , \tag{2.10}$$

where the g_K are solutions of the variational system of equations

$$\sum_{K'}(H^L_{KK'}-EN^L_{KK'})g_{K'}=0\ . \tag{2.11}$$

The matrix elements are given by

$$H^L_{KK'}=\frac{2L+1}{8\pi^2}\int D^{L*}_{KK'}(\Omega)\langle\Psi_\omega|\hat{H}\hat{R}(\Omega)|\Psi_\omega\rangle d\Omega\ , \tag{2.12}$$

and by a similar expression for $N^L_{KK'}$. According to the parity of L, system (2.11) has $L+1$ or L eigenvalues E_{Li}. Besides the lowest one E_{L0}, other low eigenvalues may have a physical meaning. In practice, for high values of L_x, the system (2.11) may be strongly redundant[6] and become difficult to solve if the matrix elements are known with a limited accuracy. In this case, a useful upper bound to the lowest eigenvalue is given by

$$E_{L0}\lesssim\min_K(H^L_{KK}/N^L_{KK})\ . \tag{2.13}$$

Because of (2.4), the matrix elements between $|\Psi_\omega\rangle$ and a rotated wave function satisfy numerous symmetry properties. Several of them will be used in Sec. III C to check the accuracy of the calculations. Let us quote here the relation

$$\langle\Phi|\hat{H}\hat{R}(\pi-\alpha,\beta,-\gamma)|\Psi\rangle=\langle\Phi|\hat{H}\hat{R}(\alpha,\beta,\gamma)|\Psi^*\rangle\ . \tag{2.14}$$

This relation allows one to reduce the number of rotations. Such a reduction is valuable since the main part of computation time is due to rotations. Using the properties (2.4) and (2.14), the integration domain in (2.12) can be reduced by a factor of 32. Moreover, this reduction allows us to avoid Euler angles larger than $\frac{1}{2}\pi$, which is important when the error introduced by an approximate rotation increases with the angle. After reduction, (2.12) takes the form

$$H^L_{KK'}=\frac{2L+1}{2\pi^2}\int_0^{\pi/2}d\alpha\int_0^{\pi/2}\sin\beta\, d\beta\int_{-\alpha}^{+\alpha}d\gamma\,\mathscr{H}^L_{KK'}(\Omega)\ , \tag{2.15}$$

with

$$\mathscr{H}^L_{KK'}(\Omega)=(f^R_{KK'}+f^R_{K'K})\mathrm{Re}[\langle\Psi_\omega|\hat{H}\hat{R}(\Omega)|\Psi_\omega\rangle+(-)^K\langle\Psi_\omega|\hat{H}\hat{R}(\Omega)|\Psi^*_\omega\rangle]\quad(K+K'\text{ even})$$

or

$$\mathscr{H}^L_{KK'}(\Omega)=(f^I_{K'K}+f^I_{KK'})\mathrm{Im}\langle\Psi_\omega|\hat{H}\hat{R}(\Omega)|\Psi_\omega\rangle+(-)^K(f^I_{K'K}-f^I_{KK'})\mathrm{Im}\langle\Psi_\omega|\hat{H}\hat{R}(\Omega)|\Psi^*_\omega\rangle\quad(K+K'\text{ odd})\ ,$$

where Re or Im denote the real or imaginary part of a c number. The real functions $f^R_{KK'}$ and $f^I_{KK'}$ are given by

$$f^R_{KK'}+if^I_{KK'}=d^L_{KK'}(\beta)e^{i(K\alpha+K'\gamma)}+(-)^L d^L_{K-K'}(\beta)e^{i(K\alpha-K'\gamma)}\ .$$

C. Calculation of matrix elements

The projection on angular momentum requires the calculation of matrix elements involving rotated functions [Eq. (2.12)]. In spite of the resulting nonorthogonality of the orbitals, the Hamiltonian matrix elements can be calculated with the usual Hartree-Fock functional provided that the modified densities

$$\rho(\vec{r},\Omega)=\sum_{ij}[\mathscr{N}^{-1}(\Omega)]_{ji}\psi^*_i(\vec{r})\hat{R}(\Omega)\psi_j(\vec{r}) \tag{2.16a}$$

and

$$\tau(\vec{r},\Omega)=\sum_{ij}[\mathscr{N}^{-1}(\Omega)]_{ji}\vec{\nabla}\psi^*_i(\vec{r})\cdot\vec{\nabla}\hat{R}(\Omega)\psi_j(\vec{r}) \tag{2.16b}$$

are used.[14] In (2.16), the overlap matrix $\mathscr{N}$ is defined by

$$\mathscr{N}_{ij}(\Omega)=\int\psi^*_i(\vec{r})\hat{R}(\Omega)\psi_j(\vec{r})d\vec{r}\ . \tag{2.17}$$

The determinant of $\mathscr{N}(\Omega)$ provides the overlap matrix elements necessary to compute $N^L_{KK'}$. Since $\hat{R}$ commutes with $\hat{P}$ but does not commute with $\hat{P}_x$, matrix $\mathscr{N}$ is composed of two diagonal blocks, one for each parity, in place of four in the case without rotations. Hence the densities (2.16) are of positive parity but do not exhibit a particular symmetry with respect to $\hat{P}_x$ and $\hat{P}_z$. These densities thus have to be calculated on half the configuration space.

III. ROTATIONS ON A MESH

A. Orbital momentum on a mesh

On a three-dimensional mesh, an individual wave function is represented by the set of its (complex) values taken at all the mesh points. In the following we shall assume that the mesh is Cartesian with a constant mesh size h and that it obeys the symmetries of the D_{2h} group. Let N_x, N_y, and N_z be the numbers of mesh points in the three directions. For each direction, two types of symmetric mesh can still be chosen, according as the number of points is even or odd. We adopt for these cases the integer or half-integer numbering shown in Fig. 1. The advantage of this numbering is that a reflection is performed by changing the sign of indices. We now have a more precise definition of the representation of an individual wave function ψ_i: it is a column matrix $\tilde{\psi}_i$ with $N_xN_yN_z$ components labeled by a set of three positive or negative integer or half-integer numbers.

On the mesh, an operator is represented by a square matrix of dimension $N_xN_yN_z$. The size of these matrices is so large that they cannot be easily handled. Fortunately, most of the necessary matrices are sparse or can be reduced by taking into account the symmetries of the mesh. Let us now specialize to the matrix approximating the orbital momentum components on a three-dimensional

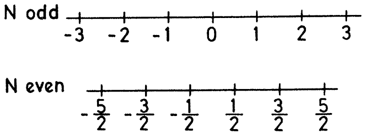

FIG. 1. Numbering of the mesh points for even and odd numbers of points.

mesh. Let us, for example, define the matrix $\tilde{L}_z$ corresponding to $\hat{L}_z$ through the matrix product

$$(\tilde{L}_z\tilde{\psi})_{lmn} = -i\sum_{\mu} c_{\mu}(l\tilde{\psi}_{lm+\mu n} - m\tilde{\psi}_{l+\mu mn}) , \tag{3.1}$$

where $c_\mu = 0$ if $|\mu| > \frac{1}{2}(N-1)$ (N odd). The coefficients c_μ of an N-point Lagrange differentiation formula[15] verify

$$c_\mu = -c_{-\mu} , \tag{3.2}$$

and are given for $N=5$, 7, and 9 in Table I [For $N=5$, see Eq. (25.3.6) of Ref. 15]. The remainder is proportional to $(\frac{1}{2}N-\frac{1}{2})!^2h^N/N!$[15] With $N=5$, (3.1) is equivalent to, but simpler than, the corresponding expression of Ref. 8. In the following, we shall use the accurate $N=9$ formula. Indeed, it will become clear that the rotation computation time is independent of N so that large values can be used. However, the value of N should remain small with respect to the numbers of mesh points in each direction.

The elements of the two-dimensional restriction of the Hermitian matrix $\tilde{L}_z$ are thus given by

$$(\tilde{L}_z)_{lm,l'm'} = -i(lc_{m'-m}\delta_{ll'} - mc_{l'-l}\delta_{mm'}) . \tag{3.3}$$

As expected, $\tilde{L}_z$ is independent of h. With (3.2), the properties

$$\begin{aligned}(\tilde{L}_z)_{lm,l'm'} &= -(\tilde{L}_z)_{-lm,-l'm'}\\ &= -(\tilde{L}_z)_{l-m,l'-m'}\\ &= (\tilde{L}_z)_{-l-m,-l'-m'}\end{aligned} \tag{3.4}$$

are readily checked. In other words, because of the symmetries imposed on the mesh, $\tilde{L}_z$ verifies the same commutation and anticommutation rules

$$[\tilde{L}_z,\tilde{P}] = \{\tilde{L}_z,\tilde{P}_x\} = \{\tilde{L}_z,\tilde{P}_y\} = 0 \tag{3.5}$$

as the exact operator. A further property of the exact operator (antisymmetry with respect to the exchange of x and y) exists only if N_x and N_y are equal. With (3.4), matrix $\tilde{L}_z$ may be written in block form

$$\tilde{L}_z = \begin{bmatrix} \tilde{L}_1 & \tilde{L}_2 & \tilde{L}_3 & \tilde{L}_4 \\ -\tilde{L}_2 & -\tilde{L}_1 & -\tilde{L}_4 & -\tilde{L}_3 \\ \tilde{L}_3 & \tilde{L}_4 & \tilde{L}_1 & \tilde{L}_2 \\ -\tilde{L}_4 & -\tilde{L}_3 & -\tilde{L}_2 & -\tilde{L}_1 \end{bmatrix} , \tag{3.6}$$

where the submatrix $\tilde{L}_r$ maps points of the rth quadrant of the xy plane into the first one. Except $\tilde{L}_1$, the matrices $\tilde{L}_r$ contain mainly zeros. ($\tilde{L}_3$ is even easily shown to vanish.) The dimension of the submatrices is about $\frac{1}{4}N_xN_y$, but care must be taken if invariant points exist, i.e., if N_x or N_y is odd. The invariant axis points must then be shared between the different $\tilde{L}_r$ to which they belong with $2^{-1/2}$ or 2^{-1} weight coefficients.

The transformation property of $\tilde{L}_z$ under time reversal

$$\{\tilde{L}_z,\hat{T}\} = 0 \tag{3.7}$$

shows that $\lambda_{\pi k}$ and $-\lambda_{\pi k}$ are simultaneous (real) eigenvalues of $\tilde{L}_z$, with complex conjugate eigenvectors $V_{\pi k}$ and $V^*_{\pi k}$. The symmetry properties of an eigenvector $V_{\pi k}$ are provided by (3.5) and (3.7):

$$\begin{aligned}&\tilde{P}V_{\pi k} = \pi V_{\pi k} ,\\ &\tilde{P}_x V_{\pi k} = \pi V^*_{\pi k} ,\\ &\tilde{P}_y V_{\pi k} = V^*_{\pi k} ,\end{aligned} \tag{3.8}$$

where π is the parity quantum number in the xy plane. The real and imaginary parts of $V_{\pi k}$ transform, respectively, according to the A_π and B_π IR of the $C_s \times C_i$ group of symmetries $\{\hat{\mathbb{1}}, \hat{P}_y, \hat{P}, \hat{P}_x\}$ in the xy plane.[13] The eigenvector $V_{\pi k}$ corresponding to an eigenvalue $\lambda_{\pi k}$ of $\tilde{L}_z$ may be written in block form

$$V_{\pi k} = 2^{-3/2}\begin{bmatrix} v_{\pi k} \\ v^*_{\pi k} \\ \pi v_{\pi k} \\ \pi v^*_{\pi k} \end{bmatrix} . \tag{3.9}$$

Now, let us introduce the auxiliary matrices

$$X_{\mathrm{IR}} = \sum_r \chi_{\mathrm{IR}}(r)\tilde{L}_r , \tag{3.10}$$

where $\chi_{\mathrm{IR}}(r)$ are characters of $C_s \times C_i$ IR's.[13] Obvious properties of the submatrices $\tilde{L}_r$ show that

$$X_{A\pi} = (X_{B\pi})^\dagger \tag{3.11}$$

where the dagger denotes Hermitian conjugation. With (3.6) and (3.9), one obtains

$$\begin{aligned}&X_{A\pi}v^R_{\pi k} = i\lambda_{\pi k}v^I_{\pi k} ,\\ &X_{B\pi}v^I_{\pi k} = -i\lambda_{\pi k}v^R_{\pi k} ,\end{aligned} \tag{3.12}$$

where R (I) denotes the real (imaginary) part of $v_{\pi k}$. Eliminating $v^I_{\pi k}$ from (3.12) leads with (3.11) to the reduced eigenvalue problem

$$[(X_{A\pi})^\dagger X_{A\pi}]v^R_{\pi k} = \lambda^2_{\pi k}v^R_{\pi k} . \tag{3.13}$$

TABLE I. Nonvanishing Lagrange coefficients $c_{|\mu|}$ for $N=5$–9.

μ N	1	2	3	4
5	$\frac{2}{3}$	$-\frac{1}{12}$		
7	$\frac{3}{4}$	$-\frac{3}{20}$	$\frac{1}{60}$	
9	$\frac{4}{5}$	$-\frac{1}{5}$	$\frac{4}{105}$	$-\frac{1}{280}$

TABLE II. Eigenvalues of $\hat{L}_z$ for a 16×16 mesh.

			$\pi=+$				
0	0	0	0	0	0	0	0
1.33912	1.41308	1.66295	$\underline{1.85111}$	$\underline{1.94817}$	1.97416	$\underline{1.98715}$	$\underline{1.99807}$
$\underline{1.99988}$	2.52569	2.82933	2.97822	3.09380	3.38346	3.68910	$\underline{3.73401}$
$\underline{3.91268}$	3.95390	$\underline{3.98090}$	$\underline{3.99791}$	4.30776	4.60787	4.80568	4.88608
5.04830	5.27798	$\underline{5.68108}$	$\underline{5.90634}$	5.94622	$\underline{5.98491}$	6.25316	6.81629
6.99321	7.14359	7.47556	$\underline{7.64132}$	$\underline{7.91089}$	7.98850	8.13901	8.83690
9.14375	9.35562	9.67689	9.76869	$\underline{9.78419}$	10.6022	10.8850	11.4162
11.7311	12.4297	13.0308	13.0978	14.1465	14.2240	17.2356	17.2381
			$\pi=-$				
0.50033	0.74189	0.86051	$\underline{0.89232}$	$\underline{0.95295}$	$\underline{0.98566}$	$\underline{0.99705}$	$\underline{0.99966}$
$\underline{0.99999}$	1.12536	1.40115	1.63048	1.68909	1.98981	2.26629	2.28845
2.53469	2.62639	2.71725	$\underline{2.87037}$	$\underline{2.96252}$	$\underline{2.99310}$	$\underline{2.99941}$	3.04291
3.40287	3.90441	4.22665	4.47840	4.69709	4.78382	$\underline{4.82193}$	$\underline{4.95452}$
$\underline{4.99397}$	5.10560	5.72580	5.73901	6.04425	$\underline{6.42534}$	$\underline{6.81159}$	6.85222
$\underline{6.96655}$	6.97001	7.00992	7.15792	7.79724	8.17743	$\underline{8.48701}$	8.67313
$\underline{8.88411}$	9.43044	9.68294	9.83139	10.3145	10.4821	10.8371	10.9508
12.0953	12.3374	13.0291	13.0955	14.1138	14.2524	17.2339	17.2398

The matrix in (3.13) is symmetric and semipositive definite. Its dimension is about $\frac{1}{4}N_xN_y$. Once the $\lambda_{\pi k}$ and $v^R_{\pi k}$ have been computed, the $v^I_{\pi k}$ can be obtained for $\lambda_{\pi k}\neq0$ from

$$v^I_{\pi k}=(i\lambda_{\pi k})^{-1}X_{A\pi}v^R_{\pi k}\ . \tag{3.14}$$

Zero eigenvalues of (3.13) are associated with the existence of invariant points. We shall show in Sec. III B that the eigenvectors corresponding to these eigenvalues do not need to be known.

As an example, the non-negative eigenvalues for the case $N_x=N_y=16$ (this number of points is typical of the ^{24}Mg ground-state band discussed in the following) are displayed in Table II. To every positive eigenvalue in Table II there corresponds a negative one. The positive- (negative-) parity eigenvalues are a real approximation of the even (odd) integer eigenvalues m of $\tilde{L}_z$, since

$$\hat{P}e^{im\varphi}=(-)^m e^{im\varphi}\ .$$

An examination of Table II shows that a significant part of the eigenvalues are close to an even (odd) integer value. Most eigenvalues, however, are not clearly related to an even or odd integer. The underlined numbers represent eigenvalues which can be considered as approximates of an integer number. Their selection is based on properties of the corresponding eigenvectors to be discussed below. The physical eigenvalues correspond, in general, to a sequence of numbers close to, and smaller than, an integer with the correct parity. Notice that in spite of their proximity to an integer, some eigenvalues like $1.97416(\pi=+)$ or $7.98850(\pi=+)$ can unambiguously be rejected by the eigenvector criterion. A part of the degenerate zero eigenvalues should also be physical, but the exact degeneracy prevents us from classifying them.

The real parts [see Eq. (3.13)] of eigenvectors corresponding to selected eigenvalues of Table II are depicted in Fig. 2. For the sake of interpretation, the 64 components of the eigenvectors are presented in an 8×8 square box. These eigenvectors can be interpreted as an approximation on an 8×8 mesh of the real part of an eigenfunction of $\hat{L}^2_z$ restricted to the first quadrant. This interpretation is confirmed by the close similarity of the solutions of Eq. (3.13) with values at the mesh points of the functions

$$\varphi_{nm}(\rho,\varphi)=(1+\delta_{m0})^{-1/2}a(8/\pi)^{1/2}[J'_m(\epsilon^{(m)}_n)]^{-1}J_m(\epsilon^{(m)}_n\rho/a)\cos m\varphi\ , \tag{3.15}$$

where $a=8$ is the size of the box and the $\epsilon^{(m)}_n$ are zeros of the Bessel functions $J_{|m|}(x)$.[15] The functions φ_{nm} are harmonic functions in a circle of radius a; they are also eigenfunctions of $\hat{L}^2_z$, $\hat{P}_x$, and $\hat{P}_y$ with eigenvalues m^2, $(-1)^m$, and $+1$. Moreover, they are normalized over one quadrant of the circle.

The nodal lines of the φ_{nm} are represented by straight lines or circles in Fig. 2. In the upper part of Fig. 2, the eigenvectors corresponding to five positive-parity eigenvalues approximating $m=2$ are presented. The n values are given by the number of nodal circles with radius $a\epsilon^{(m)}_{n'}/\epsilon^{(m)}_n$ $(n'<n)$. A rather different example is presented in the lower part of Fig. 2. The eigenvectors corresponding to the best approximation of odd m values between 1 and 9 clearly exhibit angular lines of nodes at the zeros of $\cos m\varphi$. The number of radial nodes is zero. It is worth noticing that the eigenvectors nearly vanish in the exterior of the circle of radius a, in spite of the completely different symmetry of the mesh.

Eigenvectors corresponding to eigenvalues without physical meaning are necessary to complete the orthogonal basis. Most of them have a non-negligible component in the exterior of the circle of radius a.

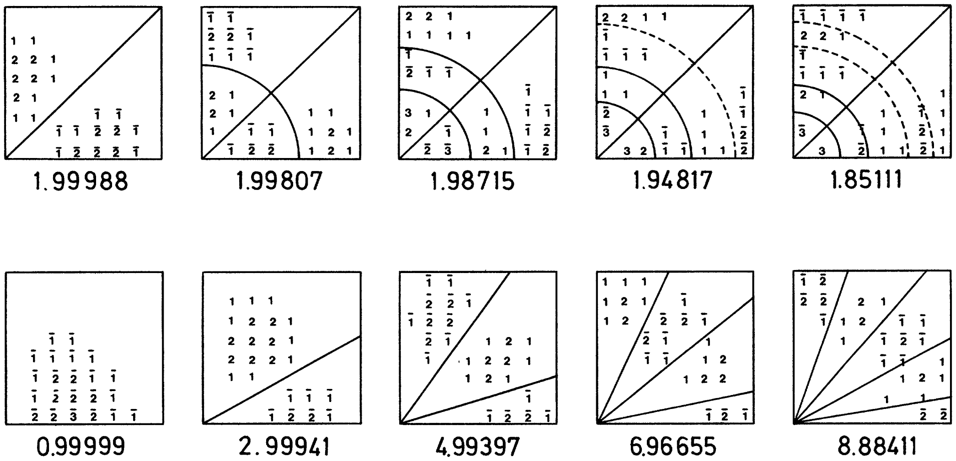

FIG. 2. Schematic representation of the normalized eigenvectors $v^R_{\pi k}$ [Eq. (3.13)] associated with eigenvalues $\lambda_{\pi k}$ of $\tilde{L}_z$ selected in Table II. The 64 components, multiplied by ten and truncated from their decimal part, are displayed in an 8×8 box corresponding to the first quadrant of the xy plane. (Negative values are surmounted by a bar.) The straight lines and circles represent, respectively, angular and radial nodal lines of the harmonic functions φ_{nm} [Eq. (3.15)]. The dashed circles have been slightly displaced from their exact location for the clarity of the figure.

B. Rotation around the z axis

First we consider rotations around one of the symmetry axes, say the z axis. The rotation operator $\hat{R}_z(\alpha)=e^{i\alpha\hat{L}_z}$ performing a rotation of angle α around this axis is approximated on the mesh by the matrix $\tilde{R}_z(\alpha)=e^{i\alpha\tilde{L}_z}$. This matrix is not sparse but can easily be computed from the eigenvalues and eigenvectors of $\tilde{L}_z$. Its size can be reduced by considering rotations in each plane $z=z_0$ separately and by taking account of symmetries of the individual wave functions. In the following, we assume that *all the individual wave functions satisfy the symmetry properties (2.4).*

For a given value z_0 of z, an individual wave function defines a complex function

$$f(x,y)=\psi_i(x,y,z_0)$$

whose properties under rotation will now be studied. Since rotations commute with the time reversal operator, the real and imaginary parts of f can be rotated separately. Rotations also commute with parity but break the other symmetry properties (2.4). Since the real and imaginary parts of f transform according to one of the four irreducible representations of the $C_s\times C_i$ group, the rotation operator can be replaced by the set of operators

$$\hat{R}_z(\alpha,\text{IR1}\to\text{IR2})=\tfrac{1}{4}[1+\chi_{\text{IR2}}(\hat{P}_y)\hat{P}_y][1+\chi_{\text{IR2}}(\hat{P})\hat{P}]e^{i\alpha\hat{L}_z}\tfrac{1}{4}[1+\chi_{\text{IR1}}(\hat{P}_y)\hat{P}_y][1+\chi_{\text{IR1}}(\hat{P})\hat{P}]\ , \qquad (3.16)$$

combining rotation and symmetry projection. Because of parity conservation, eight of the sixteen operators (3.16) vanish. Moreover, for a function of given symmetry A_π or B_π only two of the operators (3.16) are necessary to rotate and project it on the two possible symmetries, A_π and B_π, with the same parity π. The main advantage of the operators (3.16) is that rotations can now be performed with functions defined in the first quadrant $x\geq 0$, $y\geq 0$ only, which on a mesh will save computer time and memory.

Let us now transpose the operators (3.16) on a mesh. Taking account of the action of $\tilde{P}$ and $\tilde{P}_y$ on the eigenvectors $V_{\pi k}$ of $\tilde{L}_z$ (3.8), one obtains eight matrices, whose elements are defined by

$$[\tilde{R}(\alpha,A_\pi\to A_\pi)]_{ij}=\delta_{ij}+\sum_k[v^R_{\pi k}]_i[\cos(\alpha\lambda_{\pi k})-1][v^R_{\pi k}]_j\ ,$$

$$\begin{aligned}[\tilde{R}(\alpha,A_\pi\to B_\pi)]_{ij}&=-[\tilde{R}(\alpha,B_\pi\to A_\pi)]_{ji}\\&=-\sum_k[v^I_{\pi k}]_i\sin(\alpha\lambda_{\pi k})[v^R_{\pi k}]_j\ ,\end{aligned} \qquad (3.17)$$

$$[\tilde{R}(\alpha,B_\pi\to B_\pi)]_{ij}=\delta_{ij}+\sum_k[v^I_{\pi k}]_i[\cos(\alpha\lambda_{\pi k})-1][v^I_{\pi k}]_j\ .$$

The expressions (3.17) are written in a form which avoids the use of eigenvectors corresponding to zero eigenvalues. The number of nonvanishing terms in the sum over k is given by the rank of matrix $X_{A\pi}(X_{A\pi})^\dagger$.

A rotation of a three-dimensional individual wave function around the z axis is performed as a succession of $\frac{1}{2}N_z$ planar rotations for the different values of z_n. Each rotation is performed with the same rotation matrix of reasonable size (i.e., about $\frac{1}{4}N_xN_y$). The rotation matrices depend continuously on the angle α but do not satisfy the uniformity properties of rotations. An example of this nonuniformity is presented in Table III. The wave function $|\Psi_\omega\rangle$ with $L_x=7.8$ belonging to the ^{24}Mg ground-state band (see Sec. IV A) is rotated by an angle $n\pi$ (n integer) around the x axis. For exact rotations, all the moduli should be identical and all the phases should vanish. Table III indicates a regular decrease of the moduli: about 1.5% for each increase of π. The error on the phase increases by 2° for each additional π.

Since the mesh is symmetric, no angles larger than $\frac{1}{2}\pi$ are necessary [see (2.15)] which limits the magnitude of the error. If the mesh exhibits the additional symmetry

TABLE III. $n\pi$ rotations around the x axis.

	$\langle\Psi\,|\,\hat{R}_x(\alpha)\,|\,\Psi\rangle$		$-\langle\Psi\,|\,\hat{H}\hat{R}_x(\alpha)\,|\,\Psi\rangle$	
α	modulus	phase	modulus	phase
0	1	0	185.72	0
π	0.983	−0.037	182.47	−0.036
2π	0.971	−0.070	180.32	−0.069
3π	0.956	−0.100	177.65	−0.099
4π	0.942	−0.128	174.87	−0.125
5π	0.933	−0.156	173.36	−0.154
6π	0.915	−0.182	170.04	−0.179
7π	0.897	−0.205	166.85	−0.202
8π	0.882	−0.225	164.01	−0.222

$N_x=N_y$, angles larger than $\frac{1}{4}\pi$ can be avoided using

$$\hat{R}_z(\alpha)=\hat{R}_z(\tfrac{1}{2}\pi)\hat{R}_z(\alpha-\tfrac{1}{2}\pi)\ . \tag{3.18}$$

In this case the $\frac{1}{2}\pi$ rotation can be obtained exactly from the exchange of the x and y coordinates.

C. Three-dimensional rotations

An arbitrary rotation of an individual wave function is obtained as a succession of three rotations around the z, y, and z axes.[16] Let us emphasize, however, a small complication arising from the $C_s\times C_i$ symmetry restoration. For given initial and final symmetries, two different paths of intermediate symmetries occur in the succession of rotations. All the possible cases are easily worked out and will not be given here.

In order to estimate the accuracy of rotations, we have studied different symmetries of the matrix elements of $\hat{R}(\Omega)$ and $\hat{H}\hat{R}(\Omega)$. Most of these symmetries are not exact on a mesh. Indeed, the angular momentum structure relations are not satisfied exactly by $\tilde{L}_x$, $\tilde{L}_y$, and $\tilde{L}_z$. The error on the structure relations is of the same order of magnitude as the error given for the Lagrange differentiation formula (3.1). In Table IV are presented typical matrix elements computed with nine equivalent formulae for the same wave function as in Table III. If the phases remain strikingly stable under the different symmetry operations, the moduli exhibit errors which reach 5%. However, two points should be kept in mind: (i) For the angles chosen, the matrix element is already rather small. Its value is about 1% of the matrix element without rotation. (ii) Except for the first and last matrix elements, the other sets of angles are out of the integration domain of (2.15). The error remains smaller than 3% if only one angle is larger than $\frac{1}{2}\pi$. Hence, we think that the maximum error in the reduced integration domain is smaller than 1% and reaches this value when the integrant is already rather small. We thus estimate the overall accuracy on the projection as much better than 1%, presumably about 0.1%.

IV. APPLICATION TO ^{24}Mg

A. Summary of cranked Hartree-Fock calculation for ^{24}Mg

In the rest of this paper, we present the results obtained by projecting on angular momentum the ^{24}Mg wave functions determined in Ref. 9. These wave functions are the solutions of the cranked HF equations on a three-dimensional mesh. A large number of bands have been followed from $L_x=0$ up to the angular momentum for which they either fission or become unstable. The main conclusions of Ref. 9 can be summarized as follows (see Fig. 3):

(i) The ground-state band remains yrast up to $L_x\approx 14$; above this point, a configuration which is excited by more than 10 MeV at $L_x=0$ becomes yrast.

(ii) Many bands lead to symmetric fission [according to (2.4a) only symmetric configurations have been considered]. No more local minima as a function of the deformation have been found above $24\hbar$

(iii) An important result obtained in the rotating harmonic oscillator model[17] (RHO) has been confirmed. It is possible to show in the RHO that the moment of inertia of a band decreases drastically beyond a critical angular momentum related to the filling of the oscillator shells. Although no basis of any kind has been used in Ref. 9, a correspondence can be made for most of the bands with RHO bands and a similar behavior is obtained at the critical angular momentum.

TABLE IV. Overlap and Hamiltonian matrix elements for different symmetry operations ($\alpha=20°$, $\beta=30°$, $\gamma=50°$).

	Overlap		Hamiltonian	
	$10^3\times$modulus	phase	modulus	phase
$\langle\Psi\,|\,\hat{R}(\alpha,\beta,\gamma)\,|\,\Psi\rangle$	9.27	−1.11	1.78	1.99
$\langle\Psi^*\,|\,\hat{R}(\alpha,\pi-\beta,-\gamma)\,|\,\Psi\rangle$	9.03	−1.08	1.72	2.02
$\langle\Psi^*\,|\,\hat{R}(-\alpha,\pi-\beta,\gamma)\,|\,\Psi\rangle$	9.03	−1.08	1.72	2.02
$\langle\Psi\,|\,\hat{R}(\pi-\alpha,\pi-\beta,\gamma)\,|\,\Psi^*\rangle$	8.80	−1.09	1.68	2.02
$\langle\Psi^*\,|\,\hat{R}(\alpha,\pi-\beta,\pi-\gamma)\,|\,\Psi\rangle$	8.79	−1.09	1.67	2.01
$\langle\Psi^*\,|\,\hat{R}(\pi+\alpha,\beta,\gamma)\,|\,\Psi\rangle$	9.47	−1.11	1.82	1.99
$\langle\Psi\,|\,\hat{R}(\alpha,\beta,\pi+\gamma)\,|\,\Psi^*\rangle$	9.47	−1.10	1.82	2.00
$\langle\Psi^*\,|\,\hat{R}(\pi+\alpha,\beta,\pi+\gamma)\,|\,\Psi^*\rangle$	9.68	−1.11	1.86	1.99
$\langle\Psi^*\,|\,\hat{R}(-\gamma,-\beta,-\alpha)\,|\,\Psi^*\rangle$	9.27	−1.11	1.79	1.99

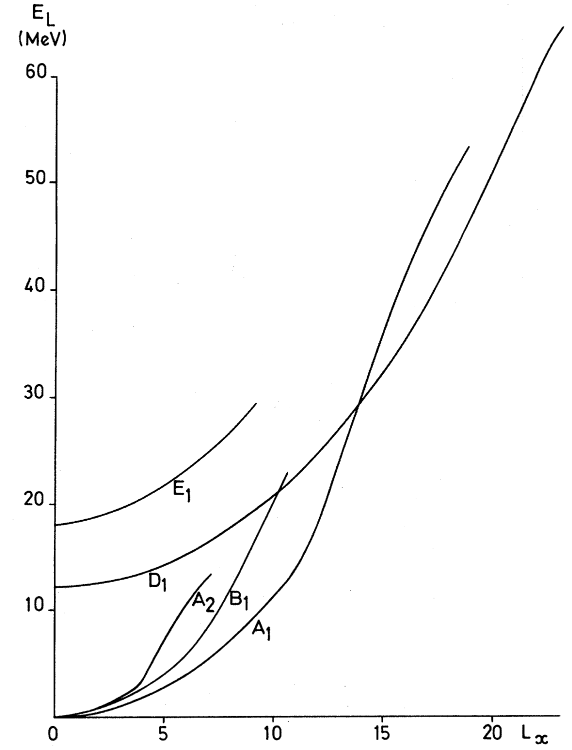

FIG. 3. Selection of ^{24}Mg rotational bands obtained in the cranking approximation and their labeling according to Fig. 3 of Ref. 9.

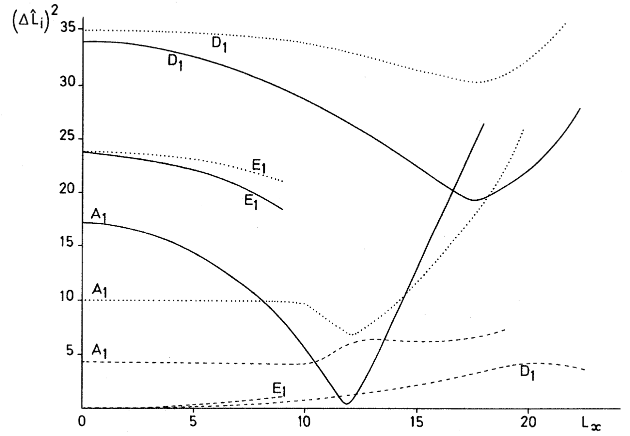

FIG. 4. Dispersions for the $A1$, $D1$, and $E1$ bands in the x (full lines), y (dotted lines), and z (dashed lines) directions.

(iv) The BKN interaction does not lead to the correct moment of inertia of the ground-state band. This could be due to the lack of spin-orbit interaction, but it is also a common feature of all the cranking calculations of ^{24}Mg.[7] This discrepancy does not permit a quantitative comparison with the experimental data.

The fourteen bands calculated in Ref. 9 correspond to different fillings of the four blocks of individual wave functions or to different minima as a function of the deformation parameters. Here, we have decided to consider only states which remain orthogonal after projection. The projection of nonorthogonal states would lead to redundant information. To obtain meaningful results would require an extra orthogonalization which is beyond our scope with a simple force like BKN. After rotation, two Slater determinants are orthogonal if they are not composed of the same numbers of positive and negative parity individual states. It is easy to check that the only bands which fulfill this condition are (according to the labeling of Ref. 9) $A1$ (three positive and three negative parity states) $D1$, (two and four, respectively), and $E1$ (four and two). Their energies are plotted as a function of L_x in Fig. 3. The ground state is triaxial and the ground-state band is obtained by a rotation along the medium axis. Rotations around the two other axes lead to bands $A2$ and $B1$ which are degenerate with $A1$ at $L_x=0$. The projection on angular momentum suppresses of course the distinction between these three bands. Band $D1$ becomes yrast around $L_x=14$ and fissions around $24\hbar$ in ^{4}He-^{16}O-^{4}He. Its projection enables us to study the effect of projection on the fission barrier

The behavior of the dispersions $\langle(\Delta\hat{L}_x)^2\rangle$, $\langle(\Delta\hat{L}_y)^2\rangle$, and $\langle(\Delta\hat{L}_z)^2\rangle$ are shown in Fig. 4 for bands $A1$, $D1$, and $E1$. The conditions of validity of cranking (1.1) are certainly met for $D1$ and $E1$. For band $A1$, the dispersion $\langle(\Delta\hat{L}_z)^2\rangle$ is never very low. The RHO critical angular momentum for this band is 12. Around this value, both conditions (1.1a) and (b) are violated.

B. Numerical computation of the projected matrix elements

The calculation of a "rotated" matrix element for a single set of Euler angles already takes a rather long computation time. A typical time on a Cyber 170/750 computer is one minute for a wave function belonging to the $A1$ band. It is therefore important to minimize the number of integration points. Using the symmetry relations, the domain of integration has been reduced in (2.15); in the Euler-angle space, this domain is half a rectangular parallelepiped. A fully parallelepipedic domain would be convenient for numerical integration. This can be achieved by introducing in (2.15) new coordinates $\alpha+\gamma$ and $\alpha-\gamma$ varying from 0 to π. The doubling of the integration domain does not cost computation time if (2.14) is utilized: the necessary matrix elements were already present in (2.15).

In the new domain, integration can be performed accurately with a triple Gauss-Legendre[15] quadrature formula. This method is suitable in the present case since the matrix elements are infinitely derivable functions of α, β, and γ [see (3.17)]. Typical numbers of points for the quadrature are 8 or 12 in band $A1$, and 4 or 6 in band $D1$ for the $\alpha+\gamma$ and $\alpha-\gamma$ coordinates. For the β coordinate, the numbers of points are larger: e.g., 8 to 24 for band $A1$ and 24 or 32 for the other bands.

In order to save computer time, it is essential to choose the most economical Gauss-Legendre formula and not to compute the integrant if it does not contribute significantly to the integral. A good choice for the quadrature formula and a first guess of the non-negligible points can be obtained from the simple approximation formula

$$\langle \hat{R}(\alpha,\beta,\gamma)\rangle \approx \exp\{-\tfrac{1}{2}(1-\cos\beta)[(\langle(\Delta\hat{L}_x)^2\rangle+\langle(\Delta\hat{L}_y)^2\rangle)-(\langle(\Delta\hat{L}_x)^2\rangle-\langle(\Delta\hat{L}_y)^2\rangle)\cos(\alpha-\gamma)]$$
$$+\tfrac{1}{2}\langle(\Delta\hat{L}_z)^2\rangle(1+\cos\beta)[\cos(\alpha+\gamma)-1]+\tfrac{1}{2}i\langle\hat{L}_x\rangle\sin\beta(\sin\alpha-\sin\gamma)\} \qquad (4.1)$$

This formula generalizes and improves similar expressions of the literature (e.g., 11.145 of Ref. 2). It is obtained with a modified version of the method of Ref. 18. The main advantage of (4.1) with respect to analogous formulas is that it gives a better β dependence around $\alpha=\frac{1}{2}\pi$, $\gamma=-\frac{1}{2}\pi$. The decrease in this region indeed depends on $\langle(\Delta\hat{L}_x)^2\rangle$ and not on $\langle(\Delta\hat{L}_y)^2\rangle$ like in other formulas. This difference is important because $\langle(\Delta\hat{L}_x)^2\rangle$ and $\langle(\Delta\hat{L}_y)^2\rangle$ differ in an appreciable way (see Fig. 4), especially for band $A1$. Equation (4.1) gives a fair first approximation of the integrant for bands $D1$ and $E1$. For band $A1$, higher order formulas have also been utilized. Besides the points selected with (4.1), small numbers of additional points need to be computed.

The total numbers of points necessary for the numerical integrations vary from less than one hundred (low states of bands $A1$ and $D1$) up to more than four hundred points for high L_x values. We have checked the accuracy of the quadrature by reprojecting the $L_x=1.8$ state of band $A1$ with higher numbers of points in the Gauss-Legendre formulas. Finally, let us notice that the heads of bands $D1$ and $E1$ correspond to axial states (i.e., eigenstates of $\hat{L}_z$ with zero eigenvalue) to a good approximation and can be projected with a one-dimensional integration over β. Unfortunately, the other members of the same bands cannot be eigenstates of $\hat{L}_z$ as soon as L_x is different from zero.

C. Comparison of projection and cranking results

We have projected five wave functions of band $A1$ ($L_x=0$, 1.8, 5.0, 7.8, and 15.7), six of $D1$ ($L_x=0$, 3.7, 7.4, 12.0, 17.3, and 20.8), and one of $E1$ ($L_x=0$). The mesh size used in all these calculations is $h=1.0$ fm. Band $E1$ being very excited, we have in this case limited our calculation to the projection of the bandhead. No state with angular momentum around $12\hbar$ has been projected for $A1$, the conditions of validity of the cranking method (1.1a) and (1.1b) being strongly violated for this angular momentum (see Fig. 4). The very low values of the dispersions in the three directions indicate that the integration of a cranking wave function in this region requires a very large number of Euler angle values. Moreover, the decomposition of the $L_x=12.0$ wave function of band $A1$ into eigenfunctions of $\hat{L}_x$ shows that its structure is very different from the structure of the other members of the band. This wave function is dominated by the $K_x=12$ component which has a weight equal to 90%, while for the other wave functions, the weight of a component is never larger than 25%. One can therefore expect that the projection on angular momentum for $L_x=12.0$ will not improve the energy obtained by the cranking method as much as for the other L_x values, and we have preferred to avoid this tedious calculation.

Since it does not require much additional work to project the wave functions corresponding to a given L_x on all the angular momenta, we have obtained for each L_x a rotational spectrum. The results are shown in Fig. 5 for band $A1$ and in Fig. 6 for band $D1$; we have drawn a straight line joining the points for each L value. If the cranking method is valid, the minimum of these curves must be obtained for each L value at $L=L_x$. One can see that this property is verified to a large extent and that deviations are small. This result is not surprising for band $D1$ which verifies conditions (1.1). However, the results obtained for $A1$ seem to indicate that the validity of the cranking method is wider than expected from (1.1). This VAP calculation is of course performed in the restricted basis composed of the cranking wave functions, but this basis covers a large range of deformations [see the trajectory in the (Q_0,γ) plane of Fig. 4 in Ref. 9].

The cranking wave functions obtained for each value of L_x can be decomposed into their L components. The probability of finding the L component can be calculated from (2.5):[2]

$$W_L=\sum_{\lambda K}|a_{\lambda LK}|^2=\sum_K N_{KK}^L\ . \qquad (4.2)$$

These probabilities are plotted in Fig. 7 for bands $A1$ and $D1$. The strength obtained for each component of band $D1$ is rather small (always less than 20%) with a

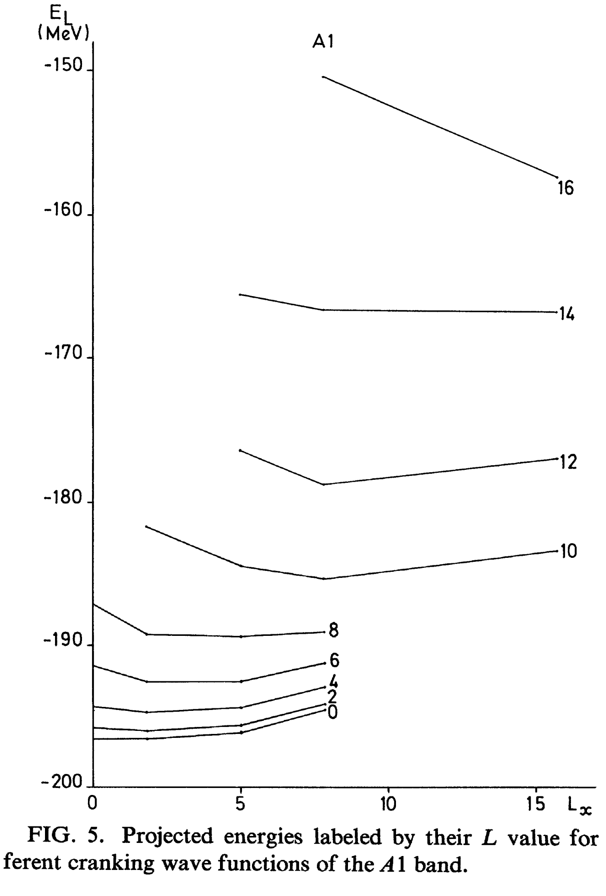

FIG. 5. Projected energies labeled by their L value for different cranking wave functions of the $A1$ band.

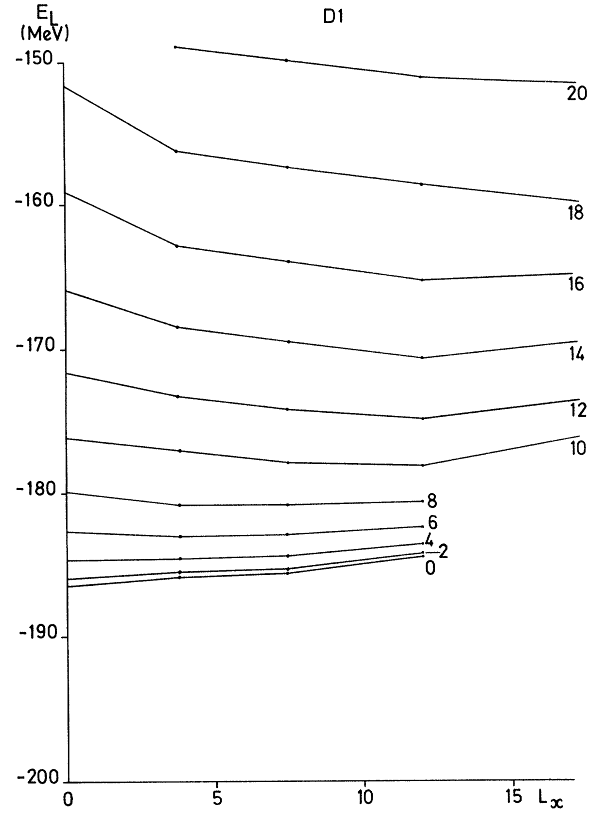

FIG. 6. Projected energies labeled by their L value for different cranking wave functions of the $D1$ band.

maximum around $L = L_x$, except if L_x is small. Beyond $L_x = 8$, all the curves present the same shape. A similar result has been obtained by Islam *et al.*[18] in an analysis of cranked HFB wave functions for ^{164}Er. In this case, as for band $D1$, the conditions (1.1) are satisfactorily met. The wave functions of band $A1$ have a very different structure. The RHO critical angular momentum for this band is $12\hbar$. This value clearly introduces a modification of the cranking wave functions (see also Fig. 4). For L_x lower than 12, the cranking wave functions have very small components beyond $L = 12$. This leads to very sharply peaked distributions when L_x is close to 12, as exemplified by the $L_x = 7.8$ wave function. The $L_x = 15.7$ wave function has a distribution of probabilities much more similar to the distributions obtained for band $D1$. Band $A1$ is not axial for $L_x = 0$. This probably explains why it is the only one to have non-negligible odd-L components (of even parity).

Conditions (1.1) ensure the accuracy of the relative energies calculated by the cranking method within a band. However, there is no guarantee that the relative energies between the bandheads are correctly predicted by the Hartree-Fock method. The lowering ΔE of the $L_x = 0$ states of bands $A1$, $D1$, and $E1$ is, respectively, 4.5, 6.4, and 5.7 MeV. As expected, the gain in energy is not the same for the three bands. However, the differences are not large compared to the excitation energies of bands $D1$ (10.0 MeV) and $E1$ (16.6 MeV) and does not change qualitatively the position of the bands.

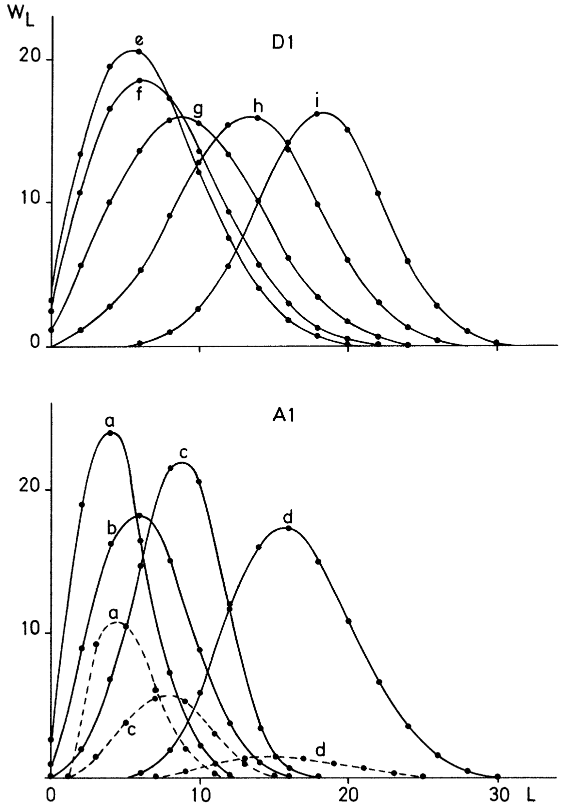

FIG. 7. Probabilities of L components [Eq. (4.2)] as a function of the angular momentum L for configurations with $L_x = 0$ (a), 5.0 (b), 7.8 (c), 15.7 (d) in the $A1$ band and with $L_x = 0$ (e), 3.7 (f), 7.4 (g), 12.0 (h), and 17.3 (i) in the $D1$ band. Full and dashed lines are drawn to guide the eye, respectively, for the even and odd L values.

The gain in energy between the intrinsic state ($L_x = 0$) and the 0^+ projected state is often estimated by[1]

$$\Delta E \approx \langle \hat{L}^2 \rangle / 2\theta \, , \tag{4.3}$$

the moment of inertia θ being extracted from the experimental spectrum. The lowering of the bandheads that we have obtained here corresponds in (4.3) to moments of inertia equal to 3.5, 5.4, and 4.2 MeV^{-1} for bands $A1$, $D1$, and $E1$, respectively, while the moments of inertia deduced from the cranking band are 5.4, 5.6, and 7.3 MeV^{-1} (these values are not qualitatively modified by the projection, as we shall see in the following). Band $D1$ is the only one for which the two values agree. This indicates that the use of (4.3) may lead to a wrong estimation of the position of the bandhead.

It can be estimated from Figs. 5 and 6 to which extent a cranking calculation previous to the projection (as an approximation of a VAP calculation) is necessary to determine accurately the energies of the different states of a band. For band $A1$, the projection of the $L_x = 0$ state leads to an energy of the 2^+ state 50 keV higher than the projection of the $L_x = 1.8$ state, while the error on the 4^+ state is already large (400 keV). The situation is more favorable for band $D1$, since the error on the 6^+ state is lower than 300 keV. One can conclude from this result that the projection of the bandhead leads to an accurate estimation of the 0^+-2^+ separation energy. The interest of this result is that the $L_x=0$ state is much easier to project than the other states of a band since it is time-reversal invariant. The numerical integration of the overlap and energy kernels also requires a smaller number of triplets of Euler angles. It is even the only wave function for which in some cases (like for bands $D1$ and $E1$) an axial integration is sufficient. This rather easy projection could be used in the future to include the 0^+-2^+ separation energy of some deformed nuclei in the fit of nuclear interactions.

D. Discussion of ^{24}Mg spectrum

The bands obtained after projection on angular momentum are shown in Fig. 8. For each value of L, we have selected the cranking wave function leading to the lowest eigenvalues (see Figs. 5 and 6). The diagonalization of Eq. (2.11) leads to $L+1$ eigenvalues for L even and to L eigenvalues for L odd. For band $D1$, the second eigenvalue is always very excited and we have only plotted the lowest one. The wave functions of band $A1$ being triaxial, the projection of this band leads for each L value to several low-energy eigenvalues. In Fig. 8 we have joined the energies which form a rotational band and labeled these bands by the L value of their bandhead.

The projection confirms qualitatively the results obtained in Ref. 9 for the ground-state band, and for bands $D1$ and $E1$. The ground-state band remains yrast up to $L=12$ (instead of 14 in the cranking calculation), a value above which it crosses band $D1$. The interest of this result is that these two bands will remain orthogonal even if one introduces the spin-orbit interaction. One can therefore predict that this crossing will remain present even if an interaction more sophisticated than BKN is used. There is no clear correspondence between the bands $B1$ and $A2$ obtained in the cranking calculation and one of the bands obtained by projecting $A1$.

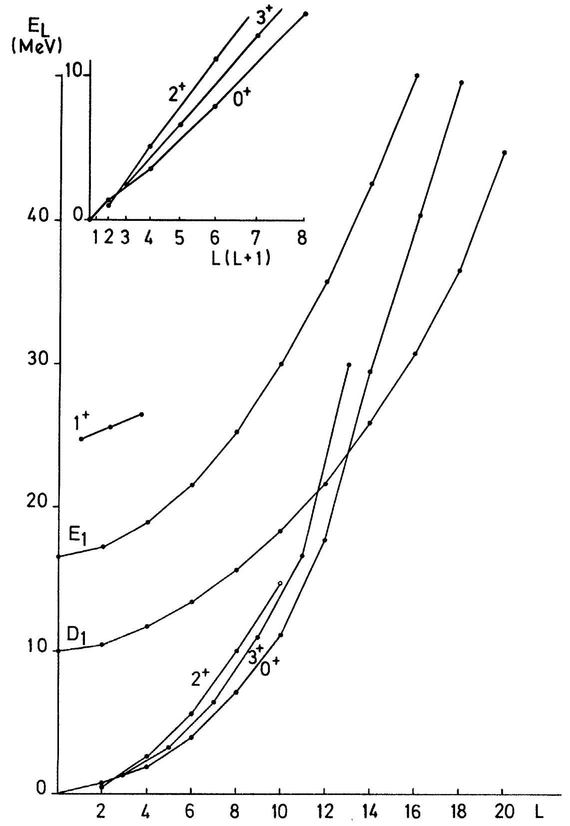

FIG. 8. VAP energies of the ^{24}Mg nucleus in the cranking space as a function of the angular momentum L. The bands 0^+-3^+ are obtained by projecting $A1$ cranking configurations. The inset displays the rotational structure of the low part of the spectrum as a function of $L(L+1)$.

The good agreement obtained here with the cranking calculation is very encouraging for the cranking method. It indicates also that the projection on good angular momentum does not improve the wrong moment of inertia obtained for the ground state band of ^{24}Mg. However, our calculation enables us to analyze the origin of this wrong moment of inertia. The 1^+ state obtained after projection is very excited; it is possible to find for each higher angular momentum an excited eigenvalue forming a band with this 1^+ state. The interpretation of the other eigenvalues is not so easy. In the inset of Fig. 8, we have plotted for $L=2$—8 the first three eigenvalues as a function of $L(L+1)$. If one considers that eigenvalues aligned along a straight line form a band, the first $L=2$ eigenvalue composes a band with the second $L=4$, 6, and 8 eigenvalues. Although K is not a good quantum number and a K value cannot be attributed to the eigenvalues of (2.11), it is tempting to relate this band to the experimentally known $K=2$ band, although it is at too low energy. The ground state will then form a band with the second $L=2$ eigenvalue and the first ones for higher even L values. The far too compressed spectrum obtained with the BKN interaction can then be related to the too low $K=2$ band which is strongly mixed with the ground-state band. The reduction of the triaxiality of the ground state would increase the gap between the bands.[19] The ^{24}Mg intrinsic state obtained in a HFB calculation[20] using the $D1$ interaction and in a HF calculation using the Skyrme force SIII indicate that the spin-orbit interaction has the desired effect. However, in both cases, the nucleus becomes axially symmetric in its ground state indicating probably too strong an effect of the spin-orbit interaction. The electric quadrupole moment obtained with the Skyrme force is smaller than the moment calculated with BKN (53 $e\,\mathrm{fm}^2$ compared to 70 $e\,\mathrm{fm}^2$). The effect of this decrease will also be to decompress the band.

E. Fission barrier

In Ref. 9, it has been found that $D1$ fissions in ^{4}He-^{16}O-^{4}He around $L_x=24$. The fission barrier can be determined by performing for each value of L_x a cranking calculation with a second constraint on the quadrupole moment. The resulting curves are shown as dashed lines in Fig. 9 for $L_x=20$, 22, and 24. To see the effect of angular momentum projection on the fission barrier, we have projected the wave functions obtained for an L_x value intermediate between 20 and 22 ($L_x=20.8$) and for three values of the quadrupole moment ($Q_0=400$, 450, and 550 fm^2). The barriers obtained for $L=18$—24 are indicated

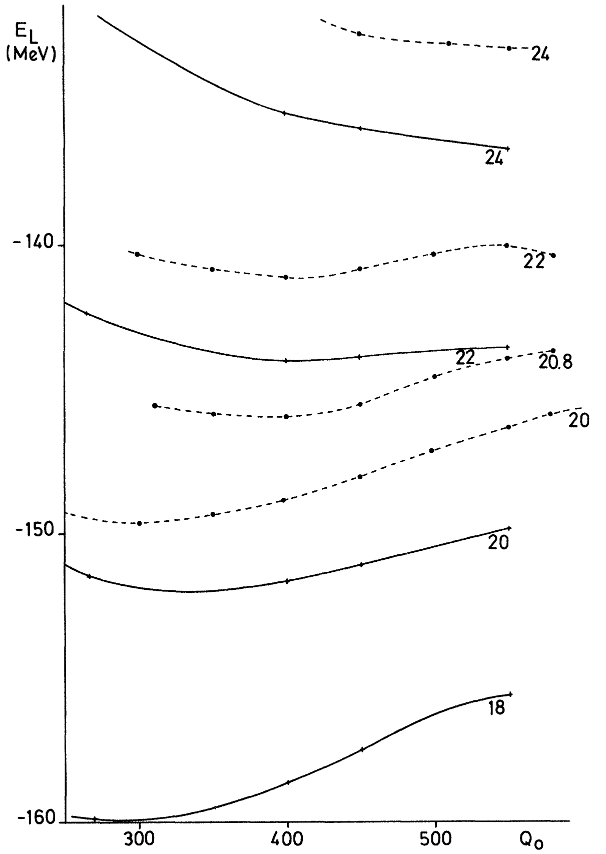

FIG. 9. ^{24}Mg fission barriers as a function of the intrinsic quadrupole moment Q_0 in the constrained cranking approximation (dashed lines, labeled by their L_x value) and as a result of the projection of the $L_x = 20.8$ cranked wave function (full lines, labeled by their L value).

as full lines in Fig. 9. We have also included in this figure the points previously calculated by projecting the $L_x = 17.3$ wave function, which corresponds to a quadrupole moment $Q_0 = 279$ fm^2. The slope of the projected barrier is slightly lower than for the cranking barrier. However, the qualitative agreement between both calculations is very good. For $L = 20$, one obtains a barrier of a few MeV; it decreases to a few hundred keV for $L = 22$ and disappears for $L = 24$.

V. CONCLUSION

We have shown in this paper that it is possible to project with a reasonable accuracy wave functions constructed on a mesh. The method proposed here is limited neither to Hartree-Fock wave functions nor to a simple nuclear interaction. The reduction of the integration domain in the Euler angles space made in Sec. II and the construction of a matrix representation for the orbital angular momentum operators made in Sec. III can be extended without major difficulties to the case of the total angular momentum $\hat{J}$. The inclusion of a spin dependence will mainly lengthen the calculation of the matrix elements but will not make its principle more complicated.

The test of the cranking method made on ^{24}Mg wave functions leads to several interesting results. The projection of band $A1$ opens the problem of validity of the cranking method. Conditions (1.1) are sufficient conditions under which the cranking method is a good approximation of a VAP calculation, but it has not been proven that they are necessary. The results obtained in the case of $A1$ seem to indicate that the validity of the cranking method is wider than deduced from (1.1). A VAP calculation using a less restricted basis than the cranking basis is of course necessary to strengthen the confidence in this assumption.

We have seen in Sec. IV D that the projection of triaxial states may lead to many bands. However, no clear connection can be made between these bands and the ones obtained by the cranking of a triaxial state around each of its three symmetry axes. Some caution seems therefore necessary in the interpretation of such bands in the cranking method. The projection of the fission barrier of band $D1$ has shown that the predictions of the cranking method for these very deformed states are quite reliable. The angular momentum of $22\hbar$ has been confirmed as the value above which the ^{24}Mg is no more stable against fission.

Another conclusion of this paper concerns the projection of the lower part of the spectrum. The projection of the $L_x = 0$ state, which is time-reversal invariant, provides a good approximation of the 0^+-2^+ separation energy. This projection being rather easy to perform, especially for axial nuclei, the 0^+-2^+ energy difference could be used as a valuable constraint on effective nuclear interactions.

ACKNOWLEDGMENTS

We would like to thank Dr. H. Flocard and Dr. M. S. Weiss for interesting discussions and comments and Prof. P. Ring for a fruitful discussion. The calculations have been performed on the CYBER 170/750 of the Brussels Free University.

---

[1] P. Quentin and H. Flocard, Annu. Rev. Nucl. Part. Sci. 28, 523 (1978); J. W. Negele, Rev. Mod. Phys. 54, 913 (1982).

[2] P. Ring and P. Schuck, *The Nuclear Many-Body Problem*, (Springer, New York, 1980).

[3] R. Y. Cusson and H. C. Lee, Nucl. Phys. A211, 429 (1973).

[4] E. Caurier and B. Grammaticos, Phys. Lett. 92B, 236 (1980).

[5] H. J. Mang, Phys. Rep. 18C, 325 (1975).

[6] K. Hara, A. Hayashi, and P. Ring, Nucl. Phys. A385, 14 (1982).

[7] M. Diebel, D. Glas, U. Mosel, and H. Chandra, Nucl. Phys. A333, 253 (1980); I. Ragnarsson, S. Åberg, and R. K. Sheline, Phys. Scr. 24, 215 (1980).

[8] H. Flocard, P.-H. Heenen, S. J. Krieger, and M. S. Weiss, Nucl. Phys. A391, 285 (1982).

[9] H. Flocard, P.-H. Heenen, S. J. Krieger, and M. S. Weiss, University of California Radiation Laboratory, Report

UCRL88504, 1982 (to be published).

[10] K. T. R. Davies, H. Flocard, S. J. Krieger, and M. S. Weiss, Nucl. Phys. A342, 111 (1980).

[11] P. Bonche, S. Koonin, and J. W. Negele, Phys. Rev. C 13, 1226 (1976).

[12] A. L. Goodman, Nucl. Phys. A230, 466 (1974).

[13] L. Landau and E. Lifchitz, *Mécanique Quantique* (MIR, Moscow, 1966).

[14] S. Marcos, H. Flocard, and P.-H. Heenen, Nucl. Phys. A410, 125 (1983).

[15] M. Abramowitz and I. A. Stegun, *Handbook of Mathematical Functions* (Dover, New York, 1965).

[16] Since N_y has been chosen even in Refs. 8 and 9, while N_x and N_z have been chosen odd, we have performed rotations around the z and x axes, with

$$\hat{R}(\alpha,\beta,\gamma)=e^{i[\alpha-(1/2)\pi]\hat{L}_z}e^{i\beta\hat{L}_x}e^{i[\gamma+(1/2)\pi]\hat{L}_z} .$$

When $N_x=N_z$, this method saves computer memory. However, the simplification arising from (3.18) may not be utilized.

[17] T. Troudet and R. Arvieu, Z. Phys. A 291, 183 (1979).

[18] S. Islam, H. J. Mang, and P. Ring, Nucl. Phys. A326, 161 (1979).

[19] P. Amiot, M. Harvey, and H. C. Lee, Phys. Lett. 56B, 26 (1975).

[20] M. Girod and B. Grammaticos, Phys. Rev. C 27, 2317 (1983).